

# H<sub>2</sub> infrared line emission across the bright side of the $\rho$ Ophiuchi main cloud<sup>★</sup>

E. Habart<sup>1</sup>, F. Boulanger<sup>1</sup>, L. Verstraete<sup>1</sup>, G. Pineau des Forêts<sup>1</sup>, E. Falgarone<sup>2</sup>, and A. Abergel<sup>1</sup>

<sup>1</sup> Institut d'Astrophysique Spatiale, Université Paris Sud, Bât. 121, 91405 Orsay Cedex, France

<sup>2</sup> LERMA, École Normale Supérieure and Observatoire de Paris, France

Received 20 July 2001 / Accepted 9 October 2002

**Abstract.** We present imaging and spectroscopic observations of dust and gas (H<sub>2</sub>) emission, obtained with ISO, from the western edge of the  $\rho$  Ophiuchi molecular cloud illuminated by the B2 star HD147889 ( $\chi \sim 400$ ). This photodissociation region (PDR) is one of the nearest PDRs to the Sun ( $d = 135 \pm 15$  pc from the stellar parallax) and the layer of UV light penetration and of H<sub>2</sub> emission is spatially resolved. It is therefore an ideal target to test the prediction of models on the integrated fluxes but also on the spatial distribution. The emission from dust heated by the external UV radiation, from collisionally excited and fluorescent H<sub>2</sub> are observed to coincide spatially. The spectroscopic data, obtained with ISO-SWS, allows us to estimate the gas temperature to be 300–345 K in the H<sub>2</sub> emitting layer, in which the ortho-to-para H<sub>2</sub> ratio is about 1 or significantly smaller than the equilibrium ratio ( $\sim 3$  at that temperature). We interpret this data with an equilibrium PDR model. In this low excitation PDR, the gas heat budget is dominated by the contribution of the photoelectric heating from very small grains and polycyclic aromatic hydrocarbons (PAHs). With the standard PAH abundance ( $[C/H]_{\text{PAH}} \approx 5 \times 10^{-5}$ ), we find that the H<sub>2</sub> formation rate  $R_f$  must be high in warm gas ( $\sim 6$  times the rate derived by Jura, 1975), in order to account for the observed H<sub>2</sub> emission. This result and the spatial coincidence between the PAHs and H<sub>2</sub> emission suggest that H<sub>2</sub> forms efficiently by chemisorption on the PAHs surface. If the latter interpretation is correct, the enhancement in  $R_f$  may also result from an increased PAH abundance: assuming that  $R_f$  scales with the PAH abundance, the observed H<sub>2</sub> excitation is well explained with  $R_f \approx 1 \times 10^{-16} \text{ cm}^3 \text{ s}^{-1}$  at  $T_{\text{gas}} = 330 \text{ K}$  ( $\sim 3$  times the rate derived by Jura 1975) and  $[C/H]_{\text{PAH}} \approx 7.5 \times 10^{-5}$ .

**Key words.** ISM: clouds – ISM: dust, extinction – atomic processes – molecular processes – radiative transfer

## 1. Introduction

The edges of interstellar molecular clouds are excited and photodissociated by stellar radiation. The transition zone between the dense, cold molecular gas and the tenuous, warm, ionized gas closer to the star is called photodissociation or photon-dominated region (for a recent review see Hollenbach & Tielens 1999). The structure of a PDR is determined primarily by the attenuation of the far-ultraviolet (FUV:  $6 < h\nu < 13.6$  eV) radiation field, as one moves from the ionization front into the PDR. The dominant process is the photodissociation of H<sub>2</sub>, the rate of which is determined by both H<sub>2</sub> self-shielding and attenuation by dust. These photodissociation regions, which reprocess much of the radiation energy emitted by young massive stars and produce a rich spectrum of infrared (IR) lines, are privileged objects to study the physical and chemical processes in the interstellar medium

(ISM). Molecular hydrogen is the simplest and most important molecule of the Universe, and although there is a consensus that H<sub>2</sub> forms on the surface of dust grains (Hollenbach & Salpeter 1971; Jura 1975; Duley & Williams 1984), the actual mechanism is not understood and the formation rate remains uncertain. ISO observations of the H<sub>2</sub> emission in PDRs may be able to put constraints on the interstellar H<sub>2</sub> formation rate.

Observations of the dust emission and H<sub>2</sub> rotational lines with ISO are bringing a new perspective on the structure and physical conditions in PDRs. On the one hand, ISO enables us to detect pure rotational transition lines of H<sub>2</sub>, which probe the temperature and density structure of the gas, that are not easily observable from the ground. On the other hand, the ISO camera provides mid-IR images of the dust emission at high angular resolution (3–6 arcsec) of illuminated edges of nearby molecular clouds (Abergel et al. 1999), which give strong constraints on the penetration of UV radiation through these clouds and on their small scale density structure.

In this paper, we present imaging and spectroscopic observations of dust and gas emission across the  $\rho$  Ophiuchi west interface (Sect. 2). A detailed comparison between ISO observations of dust and gas, in conjunction with ground-based near-IR imaging, and theoretical model calculations (Sect. 3) allows

Send offprint requests to: E. Habart,  
e-mail: emilie.habart@ias.u-psud.fr

<sup>★</sup> Based on observations with ISO, an ESA project with instruments funded by ESA Member States (especially the PI countries: France, Germany, the Netherlands and the United Kingdom) and with the participation of ISAS and NASA.

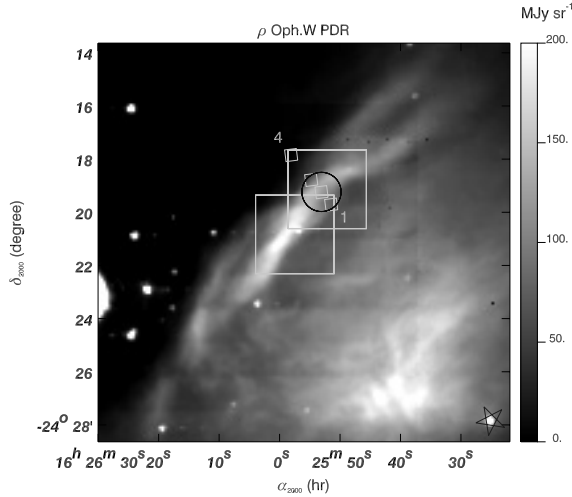


**Fig. 1.** ISOCAM map, with the LW2 filter (5–8.5  $\mu\text{m}$ ), of the bright filament along the western edge of the  $\rho$  Ophiuchi main cloud (Abergel et al. 1996). The filament is immersed in the radiation field of the star HD147889 (see the star sign). The four SWS positions (small squares), the LWS position (circle) and the CVF and ESO (more to the south) map positions are marked (big squares). The symbol sizes represent the field of view of each of these observations. The infrared emission peak observed between the star and the filament may result from a face-on PDR.

us to discuss important issues such as the penetration of ultraviolet light, the H<sub>2</sub> formation rate and the abundance of small dust grains. The paper conclusions are summarized in Sect. 4.

## 2. Observations

The  $\rho$  Ophiuchi main cloud L1688 is one of the nearest star forming regions. It contains a large number of Young Stellar Objects (YSOs) identified by ISOCAM and previous surveys (Bontemps et al. 1998). In the mid-IR image of the dust emission made with the ISO camera (Fig. 1, Abergel et al. 1996), the western edge of the L1688 cloud is delineated by a long filament located at the edge of the dense molecular gas as traced by its <sup>13</sup>CO(1–0) emission (Loren 1989). The  $\rho$  Ophiuchi West interface, centered at  $\alpha \sim 16^{\text{h}} 25^{\text{m}} 57^{\text{s}}$  and  $\delta \sim -24^{\circ} 20' 50''$  (Epoch 2000) and hereafter called  $\rho$  Oph-W, has an edge-on geometry with respect to the star HD147889 (see Fig. 1). Abergel et al. (1999) have shown that emission from small-scale structures are mainly due to dust locally heated by embedded B stars, while the large scale emission is due to external heating. The B2 star HD147889, which appears to be the center of a more-or-less spherical cavity, is the main heating source in this region (Abergel et al. 1999; Liseau et al. 1999). The bright filament presents interlaced structures likely due to the irregular shape of the edge of this cavity. We discuss the geometry and the incident radiation field of the  $\rho$  Oph-W PDR in Sect. 3.1.

### 2.1. Imaging observations of dust and gas emission

#### 2.1.1. ISOCAM imaging

An ISOCAM survey of the  $\rho$  Ophiuchi main cloud L1688 (0.5 square degrees) has been conducted in the broad-band

filter LW2 (5–8.5  $\mu\text{m}$ ) with an angular resolution of 6 arcsec (Abergel et al. 1996). Figure 1 shows the ISOCAM map in the LW2 filter of the  $\rho$  Oph-W PDR. The data processing method used is described in Abergel et al. (1999). We removed the zodiacal emission at the time of the observations using the model of Kelsall et al. (1998) based on the DIRBE/COBE data.

Spectral observations carried out with the Circular Variable Filter (CVF) of the ISO camera show that the LW2 emission is dominated by the dust features considered to be characteristic of aromatic hydrocarbons emitting during temperature fluctuations (Boulanger et al. 1998c). The interstellar particles at the origin of this emission are hereafter referred to as PAHs (Polycyclic Aromatic Hydrocarbons). This is a generic term which encompasses large aromatic molecules and tiny carbonaceous dust grains containing up to a few 100 atoms and with radii of a few  $\text{\AA}$  to a few tens of  $\text{\AA}$ . The emission at longer wavelengths arises from grains with radii ranging from 10 to 100  $\text{\AA}$ , called Very Small Grains (VSGs) which also fluctuate in temperature (Désert et al. 1990; Dwek et al. 1997; Draine & Li 2001; Li & Draine 2001). In the following, we will talk about the small grains, a term which refers to both PAHs and VSGs. Larger grains (radii  $> 0.01 \mu\text{m}$ ) which are responsible for the emission at  $\lambda \gtrsim 50 \mu\text{m}$  will be called big grains.

#### 2.1.2. ESO observation

Using the European Southern Observatory (ESO) 3.6-m telescope at La Silla, we have obtained an image in the 1–0 S(1) emission line of H<sub>2</sub> at 2.121  $\mu\text{m}$  and in the adjacent continuum filter over a small section of the bright filament (see Fig. 2). The pixel size is 0.29'' yielding a total field of  $\sim 1.5' \times 1.5'$ . Observation and data reduction were performed using standard procedures and routines for near-IR imaging. A set of frames slightly offset in telescope position have been obtained. They have been realigned and co-added to produce the final image. The sky subtraction was complicated by the presence of many bright IR sources in the  $\rho$  Ophiuchi area. The off-positions used for sky subtraction contain several sources and non-exact cancellation of these sources between the two filters produce some artefact in the final image: the bright spots at the bottom of the image and to the east of the filament do not correspond to H<sub>2</sub> emission.

The 1–0 S(1) H<sub>2</sub> emission is shown to delineate a surprisingly smooth and well resolved filament spatially coincident with the dust emission (see Figs. 2 and 5). This is unlike observations of the brighter PDRs NGC 7023 and NGC 2023 which show contrasted structures down to scales as small as 75 AU (0.5'' at the distance of  $\rho$  Ophiuchi, Lemaire et al. 1996; Rouan et al. 1997; Field et al. 1998).

## 2.2. Spectroscopic observations of gas emission

### 2.2.1. SWS observations

A significant contribution of ISO to our understanding of PDRs is due to its ability to observe with the Short Wavelength Spectrometer (SWS, Kessler et al. 1996) a series of pure rotational transition lines of molecular hydrogen. Before ISO, only

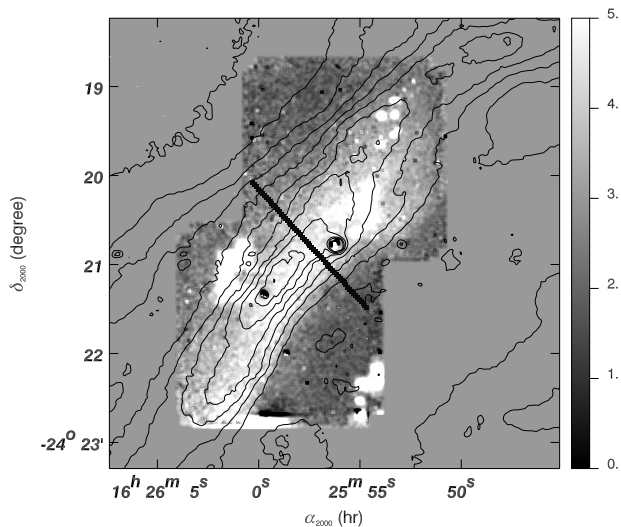


**Fig. 2.** A map of the bright filament of the western edge of the  $\rho$  Ophiuchi main cloud in the 1-0 S(1) H<sub>2</sub> emission line (in  $10^{-5}$  erg s<sup>-1</sup> cm<sup>-2</sup> sr<sup>-1</sup>) obtained at ESO (grey scale). Contours of PAH emission in the LW2 filter are superposed. The brightness profile along the cut marked here is shown in Fig. 5.

the 0-0 S(1) and the S(2) lines had been detected towards a PDR – the Orion Bar (Parmar et al. 1991).

The rotational (0-0 S(0) through to S(5)) and rovibrational (1-0 Q(1), 2-1 O(3) and 3-2 O(4)) lines of H<sub>2</sub> have been observed with the SWS across the  $\rho$  Oph-W PDR at positions marked in Fig. 1. Figure 3 shows the line spectrum observed towards position 2 and, in Table 1, we give the integrated line intensities with  $1\sigma$  error bars. The resolving power ranges from 1500 to 2500 (Valentijn et al. 1996). We applied the SWS pipeline version 7 for standard data reduction. Line intensities and error bars were obtained by fitting a Gaussian and a linear baseline to the profiles. When the signal-to-noise ratio was good enough, the fits were performed on unsmoothed data. The H<sub>2</sub> excitation diagrams, derived from the line fluxes, are shown in Fig. 4 at each SWS position, for the vibrational ground state ( $v = 0$ ). The data has been corrected for dust attenuation using the extinction curve of 1989 and a model visual extinction of 10 (see Sect. 3).

The ( $v, J$ ) excited states of H<sub>2</sub> can be populated by inelastic collisions with gas phase species, UV pumping and by the formation process on grains. For the physical conditions prevailing in bright PDRs ( $n_{\text{H}} \gtrsim 10^4$  cm<sup>-3</sup>,  $T_{\text{gas}} \sim$  a few 100 K), collisions are expected to maintain the lowest rotational levels of H<sub>2</sub> ( $v = 0, J \lesssim 5$ ) in thermal equilibrium (Le Bourlot et al. 1999). The population of these levels is therefore a good indicator of the gas temperature. We show in Fig. 4 the excitation diagrams for the  $2 \leq J \leq 7$  rotational levels of H<sub>2</sub> at the various SWS positions. In these log-log diagrams, the population of the upper level of the transition,  $N_{\text{u}}$ , is plotted against the energy of the upper level,  $E_{\text{u}}$ . When the lowest levels are thermalized by collisions, their populations should come a straight line with a slope proportional to  $1/T_{\text{gas}}$ . We see in Fig. 4 that the rotational H<sub>2</sub> levels fall on a straight line for an ortho-to-para ratio,  $R_{\text{op}}$ , equal to 1. This  $R_{\text{op}}$  value is significantly smaller

than the equilibrium ratio of 3 expected in gas at these temperatures. We discuss in Sect. 3.5 this low H<sub>2</sub> ortho-to-para ratio. The corresponding gas temperatures range from  $280 \pm 30$  K to  $330 \pm 15$  K.

Higher excitation states of H<sub>2</sub> (rotational states with  $J > 5$  and rovibrational states, see Figs. 10 and 12) are predominantly populated by the decay of electronically excited states which are pumped through the absorption of FUV photons. Therefore, the population of these levels does not depend much on the gas temperature.

### 2.2.2. ISOCAM-CVF spectro-imaging

A small fraction of the bright filament has been observed with ISOCAM in the CVF mode. The camera has been pointed to  $\alpha = 16^{\text{h}} 25^{\text{m}} 52^{\text{s}}$  and  $\delta = -24^{\circ} 19' 08''$  (Epoch 2000) with a pixel size of  $6''$ , representing a total field of  $3' \times 3'$ . The data reduction method used is presented in Boulanger et al. (1996).

The CVF mean emission spectra of the  $\rho$  Oph-W PDR (Boulanger 1998) is dominated by the dust features. As shown by Boulanger et al. (1998c) the CVF spectra can be very accurately fit by a set of five Lorentz curves centered at the position of the 6.2, 7.7, 8.6, 11.3 and 12.7  $\mu\text{m}$  features. Due to the low spectral resolution ( $\sim 40$ ), it is difficult to identify the pure rotational lines of molecular hydrogen (0-0 S(2) to S(8) transitions) within the CVF wavelength range. The 0-0 S(3) H<sub>2</sub> line at 9.66  $\mu\text{m}$ , which lies away from the PAH features, is the easiest to extract from the CVF data. Information also exist on other lines but we just present here the emission in the 0-0 S(3) H<sub>2</sub> line. We obtain the flux of the 0-0 S(3) H<sub>2</sub> line by fitting a Gaussian and a linear baseline to the line profile, after subtraction of the PAH features modelled by Lorentz profiles. Figure 5 shows the resulting 0-0 S(3) H<sub>2</sub> line profile along the cut going through the 4 positions of the SWS observations. The good match between the CVF and SWS line profiles validates the method described above to extract the 0-0 S(3) H<sub>2</sub> line flux.

In Fig. 5, we compare the brightness profile of the 0-0 S(3) and the 1-0 S(1) H<sub>2</sub> lines to the PAH emission in the LW2 filter. The H<sub>2</sub> rotational and rovibrational lines emission coincide spatially with the PAHs emission. This coincidence, also observed in other PDRs (Le Coupanec 1998; Joblin et al. 2000; An & Sellgren 2001; Habart et al. 2002a), suggests that the emission from aromatic dust heated by external UV radiation and from collisionally and fluorescent H<sub>2</sub> are closely associated. Assuming that the ratio between the emission peak of the 1-0 S(1) H<sub>2</sub> line and of the PAH in the LW2 filter is constant along the  $\rho$  Oph-W filament<sup>1</sup>, we have derived the 1-0 S(1) H<sub>2</sub> line emission through the SWS positions (see Table 1 and Fig. 11): it corresponds to the ESO brightness cut scaled by the PAH emission, e.g. multiplied by a factor of 2/3 which represents the variation of the PAH emission in the LW2 filter between the cut in the ESO map and the SWS cut.

<sup>1</sup> In other words, we assume that the physical conditions (incident radiation field, gas density) are similar between the ESO and SWS cuts. We believe that the variation of the PAH emission along the filament are mostly due to geometry effects.

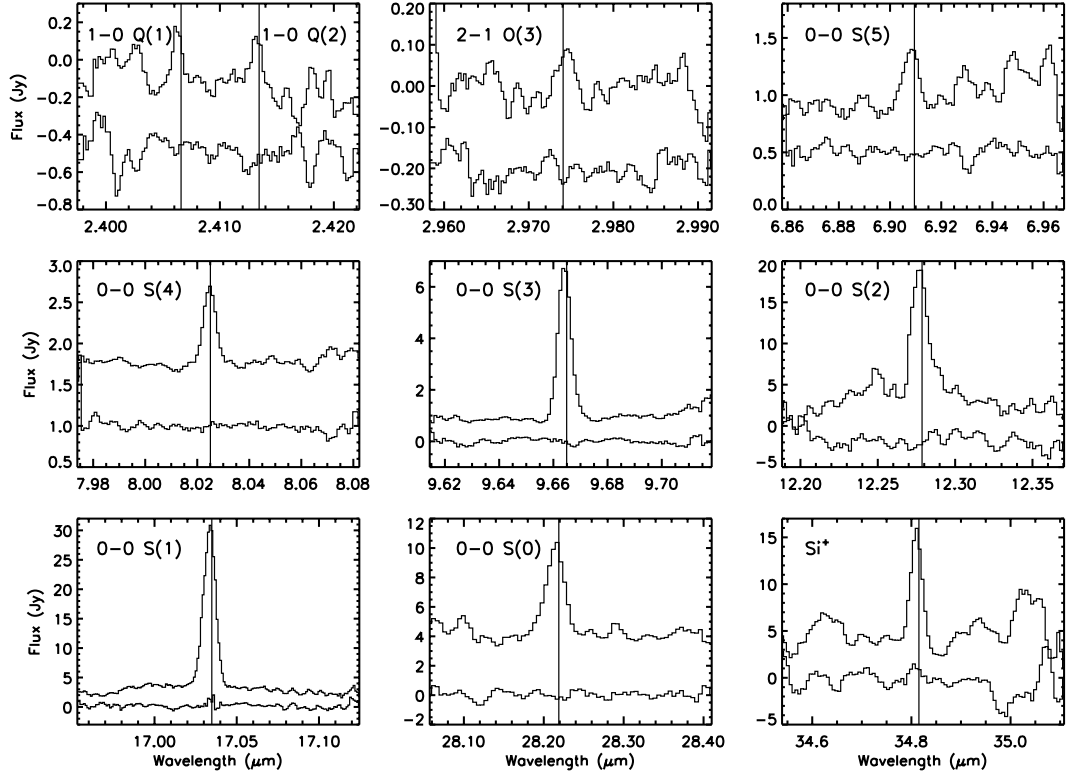


**Fig. 3.** The emission lines detected by ISO-SWS in its AOT2 observing mode towards position 2 in the  $\rho$  Oph-W interface. In each panel, the line spectrum is shown as well as the local rms noise (for clarity, an arbitrary offset value has been added to the noise). The local rms noise has been estimated from  $(UP-DOWN)/2$ : UP is the line scan where the wavelength increases with time and DOWN is the line scan where the line decreases with time (De Graauw et al. 1996). With increasing wavelength, the first two panels show H<sub>2</sub> rovibrational lines. The next six panels show pure rotational lines of H<sub>2</sub>. The last panel shows the  $^2P_{3/2} \rightarrow ^2P_{1/2}$  fine-structure line of the silicon ion.

**Table 1.** H<sub>2</sub> line intensities observed towards the  $\rho$  Oph-W PDR.

Line	$T_u^a$ (K)	$\lambda$ ( $\mu\text{m}$ )	Intensity <sup>b</sup>			
			Pos. 1	Pos. 2	Pos. 3	Pos. 4
3-2 O(4)	17389	3.39	$\leq 2.3$	$\leq 2.1$	$\leq 1$	$\leq 1.4$
2-1 O(3)	11790	2.97	1.1[10]	1.7[13]	$\leq 0.6$	$\leq 1$
1-0 S(1) <sup>c</sup>	6952	2.12	1.2[40]	3.1[16]	2.5[20]	-
1-0 Q(1)	6149	2.406	3.5[30]	2.8[20]	$\leq 1.1$	$\leq 2.2$
0-0 S(5)	4587	6.91	$\leq 1.6$	3.3[20]	1.5[22]	$\leq 0.5$
0-0 S(4)	3475	8.02	1.3[6]	3.7[22]	1.4[14]	$\leq 0.6$
0-0 S(3)	2504	9.66	7.8[10]	13.7[8]	4.4[12]	0.7[30]
0-0 S(2)	1682	12.27	12.8[33]	41.9[16]	18.4[10]	$\leq 3.8$
0-0 S(1)	1015	17.03	13.9[5]	28[19]	14.3[3]	3.3[10]
0-0 S(0)	510	28.22	2.1[9]	5.4[22]	4.7[9]	1.8[22]

<sup>a</sup> Energy of the upper level in Kelvin.

<sup>b</sup> Intensities in  $10^{-5}$  erg s<sup>-1</sup> cm<sup>-2</sup> sr<sup>-1</sup> at each SWS positions with relative uncertainty in % (in between brackets).

<sup>c</sup> For the intensity of 2.12  $\mu\text{m}$  line see text in Sect. 2.2.2.

### 3. Modelling the gas line emission

We now compare in detail the spectroscopic and imaging observations of the  $\rho$  Oph-W interface to the results of a theoretical model. We use an updated version of the PDR model of Le Bourlot et al. (1993). The key ingredients of this model are the incident radiation field at the cloud surface and the density profile across the PDR. In the following, we describe the specific geometry of this PDR and how these parameters are

constrained, in order to provide a realistic model of the  $\rho$  Oph-W PDR and further to discuss the formation of H<sub>2</sub> in PDRs.

#### 3.1. Geometry and physical conditions of the $\rho$ Oph-W PDR

The  $\rho$  Oph-W PDR is heated by the star HD147889 situated at a projected distance of 0.4 pc. ISO observations (Abergel et al. 1999; Liseau et al. 1999) show that this star has created a cavity in its surrounding due to its UV eroding radiation. Therefore,

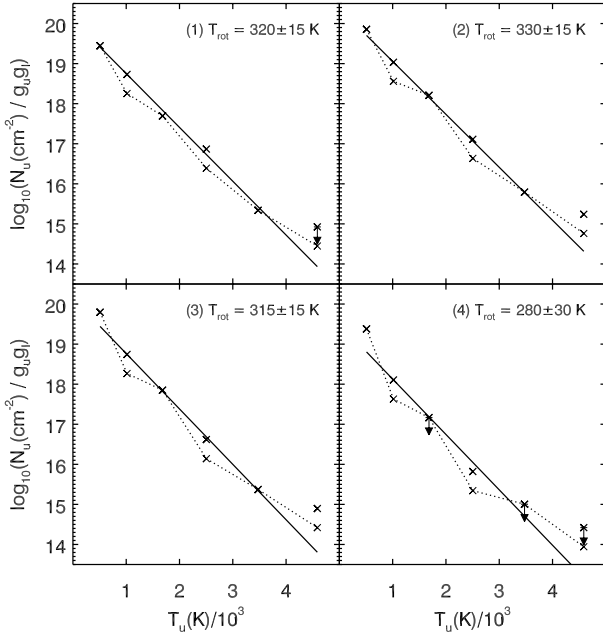


**Fig. 4.** The excitation diagrams of H<sub>2</sub> at each SWS position:  $N_u$  is the column density of the transition upper level,  $g_u$  is the degeneracy of the upper level and  $T_u$  is the upper level energy in Kelvin. The arrows indicate upper limits and the error bars are small of size comparable to the symbol size. The solid lines are rotational temperature ( $T_{\text{rot}}$ ) thermal distribution for  $R_{\text{op}} = 1$ .

we assume for the data modelling that the  $\rho$  Oph-W PDR is a piece of spherical shell (Fig. 6).

The HD147889 star is a B2V star, with a luminosity of  $\sim 5300 L_{\odot}$  and an effective temperature of 22 000 K (Liseau et al. 1999). We characterize the radiation field with  $\chi$ , a scaling factor which represents the strength of the radiation field at  $\lambda = 1000 \text{ \AA}$  in units of  $1.6 \times 10^{-3} \text{ erg s}^{-1} \text{ cm}^{-2}$  (Habing 1968). From the projected distance between the star and the interface,  $d_{\text{proj}} \sim 0.4 \text{ pc}$ , and the spectral type of HD147889, we estimate the strength of the UV exciting radiation field,  $\chi \sim 400$ .

To determine the gas density towards the  $\rho$  Oph-W PDR, we model the LW2 emission shown in Fig. 7. The brightness in the LW2 band is due mostly to PAHs (Boulanger et al. 1998c). The emission of PAHs is expected to scale with the intensity of the radiation field represented here by  $\chi$  (Puget et al. 1985; Sellgren et al. 1985). The scaling law has been verified over a wide range of  $\chi$ -values ( $\chi = 1$  to  $10^5$ ) with the help of ISOCAM-CVF data Boulanger et al. (1998a). Moreover, the PAH emission scales with the column density of PAHs. Then, along a given line of sight, the PAH emission in the LW2 filter (in  $\text{erg s}^{-1} \text{ cm}^{-2} \text{ sr}^{-1}$ ) can be written as:

$$I_{\text{LW2}}(z) = \sum_i \frac{J_{\text{LW2}}(i)}{4\pi} \times l(i) \quad (1)$$

with

$$J_{\text{LW2}}(i) = \chi \exp\left(-\sigma_{\text{UV}} \int_0^{r(i)} n_{\text{H}}(r') dr'\right) \times n_{\text{H}}(i) \times \epsilon_{\text{LW2}} \quad (2)$$

where  $i$  labels the various layer crossed by the line of sight (each layer is centered around one LW2 data point);  $l(i)$  is the

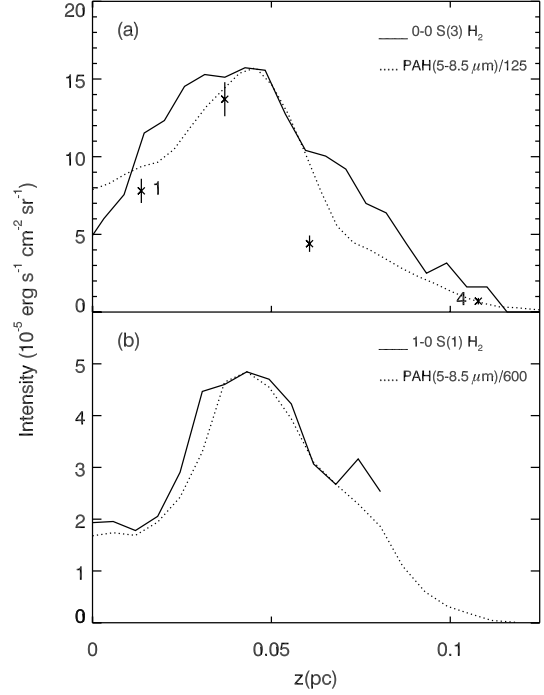


**Fig. 5.** **a)** ISOCAM-CVF brightness profile of the 0-0 S(3) H<sub>2</sub> line (solid line) along the cut going through the SWS pointings. The crosses represent the intensity of the 0-0 S(3) H<sub>2</sub> line measured by SWS with error bars. **b)** ESO brightness profile of the 1-0 S(1) H<sub>2</sub> line (solid line) along the cut shown in Fig. 2. The PAH emission in the LW2 filter along the same cuts is also shown (dotted lines). The star HD147889 lies at  $z = -0.4 \text{ pc}$  to the left of the data cut.

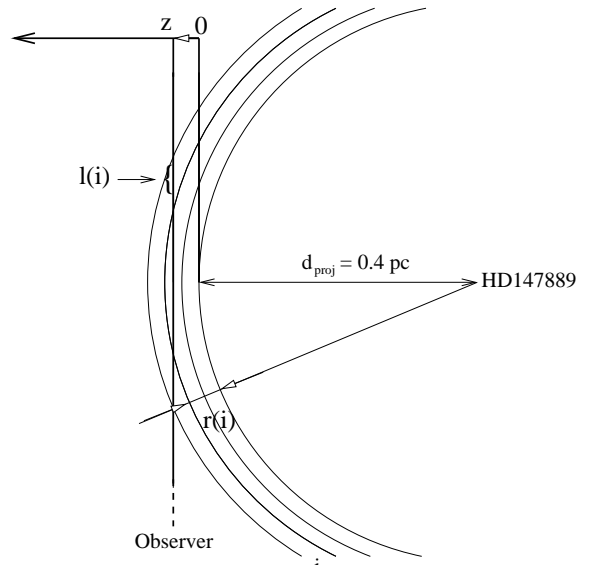


**Fig. 6.** Concave geometry used to model the  $\rho$  Oph-W PDR. Index  $i$  labels the  $A_v$ -layers of the PDR model (see Sect. 3.2).

length of layer  $i$  taken along the line of sight;  $r(i)$  is the radial depth of layer  $i$  with respect to the outer edge of the PDR facing the star (see Fig. 6),  $n_{\text{H}}(i)$  is the gas density in layer  $i$  and  $\sigma_{\text{UV}}$  ( $1.5 \times 10^{-21} \text{ cm}^2 \text{ H}^{-1}$ ) is the dust extinction cross-section at

1000 Å. Finally,  $\epsilon_{\text{LW2}}$  is the power emitted by PAHs per hydrogen atom in the LW2 filter. With this geometry, the  $\rho$  Oph-W PDR has a depth of 0.2 pc along the line of sight.

Equation (2) assumes that (i) the incident radiation field is attenuated with an effective optical depth corresponding to the dust extinction cross-section at 1000 Å (this latter has been taken constant across the PDR); (ii) the optical properties and the abundance of PAHs are constant everywhere, i.e.,  $\epsilon_{\text{LW2}}$  is a constant across the PDR. To check the validity of the first assumption, we performed the proper calculation which uses the full wavelength dependence of the dust extinction (instead of an effective value  $\sigma_{\text{UV}}$ ): we found results very similar to those obtained with Eq. (2) and conclude that this assumption is fully valid.

Based on Eq. (2), the LW2 emission profile can be interpreted as follows. From the illuminated edge of the shell (within  $\tau_{\text{UV}} < 1$ ), the brightness increase is due to a rising density, while the brightness decrease in the direction opposite to the star is due to the extinction of the incident UV radiation field. The peak position and the brightness fall are well reproduced with a density law  $n_{\text{H}}(r) \propto r^{-2.5}$  corresponding to  $1.5 \times 10^4 \text{ cm}^{-3}$  at  $A_{\text{V}} \simeq 0.5$ . The dotted line in the Fig. 7 corresponds to the profile computed with the density distribution shown in Fig. 8 and  $\epsilon_{\text{LW2}} \simeq 3 \times 10^{-32} \text{ W/H}$ . The precise shape of the density profile is not critical for the modelling of the H<sub>2</sub> line emission, which depends mainly on the density of  $1.5 \times 10^4 \text{ cm}^{-3}$  at the emission peak. In fact to constrain the gas density inside the PDR ( $A_{\text{V}} > 1$ , dashed line in Fig. 8), we have used CSO observations in the CI and CO lines (Habart 2001). The emissivity of aromatic particles in the LW2 filter deduced here ( $\epsilon_{\text{LW2}} \simeq 3 \times 10^{-32} \text{ W/H}$ ) is roughly similar to the value observed in the L1721 PDR also heated by a B2 star (Habart et al. 2001). This agreement shows that the length of the PDR ( $\sim 0.2$  pc) along the line of sight used in our spherical geometry (Fig. 6) is reasonable.

### 3.2. PDR model

We now compare the present observations of gas line emission (in particular H<sub>2</sub>) to the results of theoretical modelling based on an updated version of the code described in Le Bourlot et al. (1993). In this stationary model, a PDR is represented by a semi-infinite plane-parallel slab with an incident radiation field at the interface characterized by  $\chi$ . The input parameters are (i)  $\chi$ , the scaling factor for the radiation field, and (ii) the density profile. With these inputs the model solves the chemical and thermal balances starting from the slab edge at each  $A_{\text{V}}$ -step in the cloud. The H<sub>2</sub> abundance results from a balance between the formation of H<sub>2</sub> on dust grains and the photodissociation of H<sub>2</sub> by FUV flux, which is attenuated by dust extinction and self-shielding in the H<sub>2</sub> lines. The H<sub>2</sub> formation rate,  $R_{\text{f}}$  ( $\text{cm}^3 \text{ s}^{-1}$ ), adopted here is a semi-empirical rate coefficient:

$$R_{\text{f}} = \gamma \times \left( \frac{T_{\text{gas}}}{100 \text{ K}} \right)^{0.5} \times S(T_{\text{gas}}) \quad (3)$$

with  $\gamma$  a numerical factor in  $\text{cm}^3 \text{ s}^{-1}$ ,  $T_{\text{gas}}$  the gas temperature and  $S$  the sticking coefficient of H<sub>2</sub> onto grains equal

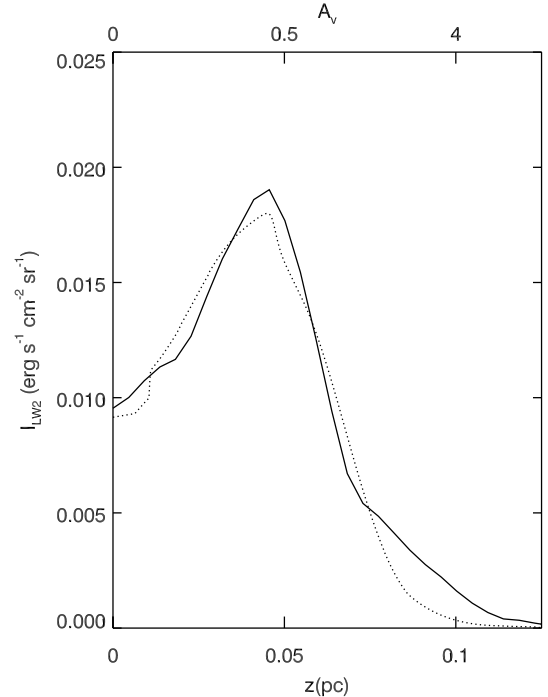


**Fig. 7.** PAH emission ( $\nu I_{\nu}(6.75 \mu\text{m})$ ) in the LW2 filter ( $5\text{--}8.5 \mu\text{m}$ ) as observed (solid lines) and predicted (dotted lines, see text) as a function of distance,  $z$ , and the visual extinction,  $A_{\text{V}}$ , integrated from the PDR outer edge. The stellar light is assumed to arrive with no extinction at  $z = 0$  pc.

to  $1/(1 + T_{\text{gas}}/400 \text{ K} + (T_{\text{gas}}/400 \text{ K})^2)$  (Burke & Hollenbach 1983; Bertoldi 1997). The standard value of  $R_{\text{f}}$  inferred from Copernicus data is  $3 \times 10^{-17} \text{ cm}^3 \text{ s}^{-1}$  (Jura 1975) at 70 K. This corresponds to  $\gamma = 4.3 \times 10^{-17} \text{ cm}^3 \text{ s}^{-1}$ . The energy of H<sub>2</sub> formation is assumed to be equally distributed between kinetic energy, internal energy of H<sub>2</sub> and heating of the grain. The radiative transfer in the absorption lines of H<sub>2</sub> and CO is treated in detail and the individual line profiles are described with the prescription of Federman et al. (1979). For the dust extinction properties, we use the analytical fit of Fitzpatrick & Masse (1988) to the HD147889 star extinction curve. The heating rate for the photoelectric effect on small dust grains (PAHs and VSGs) is derived from the formalism of Bakes & Tielens (1994). The exponent of the power law size distribution of the small grains is  $-3.5$  while the lower and upper limits of the grain radius are 4 and 100 Å respectively. The carbon locked up in PAHs ( $a \lesssim 10 \text{ Å}$ ) has an abundance of  $[\text{C}/\text{H}]_{\text{PAH}} \simeq 5 \times 10^{-5}$  inferred from the  $12 \mu\text{m}$  emission per hydrogen in typical Galactic cirrus (Boulanger & Perault 1988) and PDR (Habart et al. 2001) and from comparison between observations of dust galactic emission and extinction with detailed model calculations (Désert et al. 1990; Dwek et al. 1997; Li & Draine 2001).

Figures 8 and 9 describe the physical state of the gas, the chemical stratification and the thermal budget of the plane-parallel model as a function of depth into the PDR. In this model, we have used  $\chi = 400$  and the density profile discussed earlier (see Sect. 3.1). In these conditions, we note that the gas heating is dominated by the photoelectric effect on dust grains

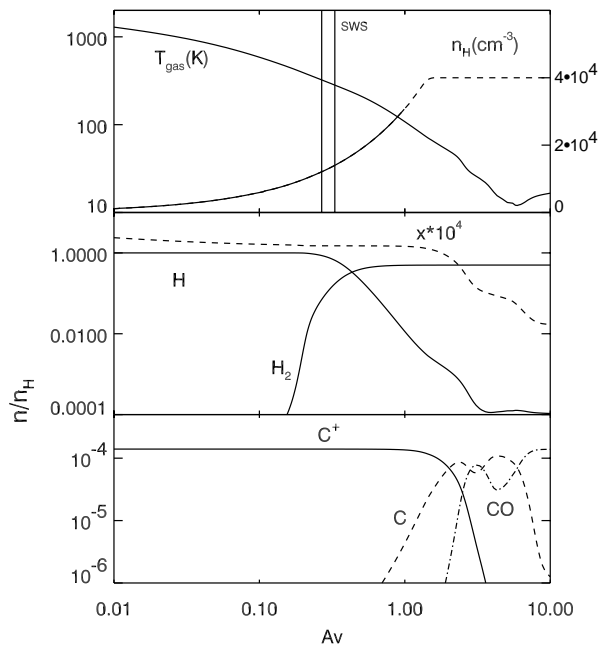


**Fig. 8.** Variation of the gas temperature, gas density and the fractional ionization  $x = n_c/n_H$  for the plane-parallel PDR model with  $\chi = 400$  and with the density profile of Sect. 3.1. We also show the H/H<sub>2</sub> and C<sup>+</sup>/C<sup>0</sup>/CO transitions for the same model characterised by a H<sub>2</sub> formation rate inferred from Copernicus data (see text).

and that the hydrogen molecule is excited by the FUV incident flux (mostly rovibrational lines) and collisions (rotational lines).

To compute the H<sub>2</sub> line intensities and the fine structure lines, we assume that the results of our plane-parallel PDR model apply along each radius of the shell (Fig. 6). As earlier, the line intensity integrated along a given line of sight is estimated from:

$$I_\nu = \sum_i \frac{J_\nu(i) \times \beta(i)}{4\pi} \times l(i) \quad (4)$$

with  $i$  labels the radial  $A_V$ -layers from the model which are crossed by the line of sight;  $l(i)$  is the length of layer  $i$  on the line of sight and  $J_\nu(i)$  is the line emissivity (in  $\text{erg s}^{-1} \text{cm}^{-3}$ ) extracted from the plane-parallel model and  $\beta$  the escape probability from layer  $i$  to the cloud edge along the line of sight. For  $\beta$ , we use the formalism of Tielens & Hollenbach (1985) in their Appendix B with a turbulent Doppler width  $\delta v_d = 1 \text{ km s}^{-1}$ . The H<sub>2</sub> rotational lines are optically thin, conversely, opacity effects are important for the fine-structure lines (see Sect. 3.6).

In the model, we impose a H<sub>2</sub> ortho-to-para ratio of 1 as suggested by the SWS data (see Sect. 2.2.1). We compare in Fig. 10 the H<sub>2</sub> line intensities as observed and as predicted at the peak of the H<sub>2</sub> emission. With a H<sub>2</sub> formation rate corresponding to  $4.3 \times 10^{-17} \text{ cm}^3 \text{ s}^{-1}$ , the observed H<sub>2</sub> line intensities are not reproduced by the PDR model. The contribution of the collisional excitation relative to UV pumping is underestimated by the model: for example the 0-0 S(3)/1-0 Q(1) line intensity ratio is predicted to be only about 1 while a value of  $\sim 5$  is observed (see Fig. 10). In fact, this model predicts that

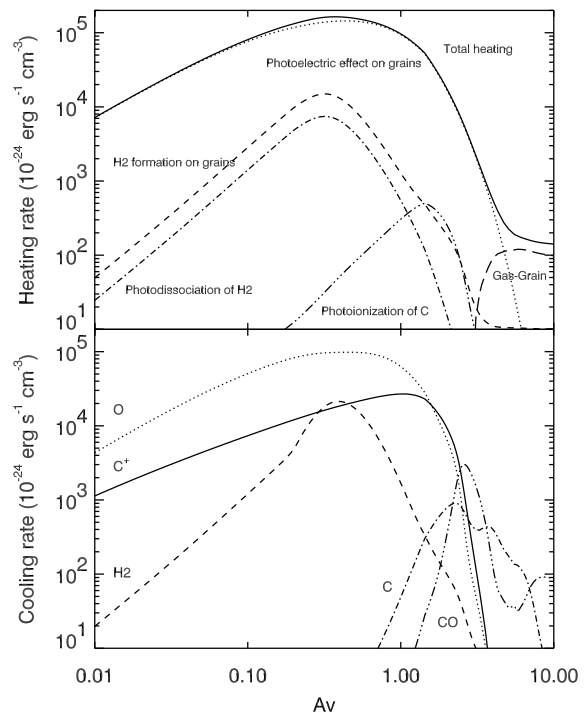


**Fig. 9.** Main heating and cooling rates for the same PDR model as in Fig. 8.

hydrogen is mostly atomic in the warm gas at the origin of the H<sub>2</sub> emission seen by SWS (Fig. 8). The H<sub>2</sub> fraction becomes appreciable deeper into the PDR ( $A_V > 0.5$ ) where the UV flux has been strongly attenuated and where the gas temperature is lower ( $T_{\text{gas}} \leq 250 \text{ K}$ ) than the excitation temperature indicated by the SWS data.

High H<sub>2</sub> excitation temperatures have been reported in other PDRs observed with ISO, e.g., S140 (Timmermann et al. 1996), NGC 7023 (Fuente et al. 1999), or NGC 2023 (Draine & Bertoldi 2000). In their modelling of the H<sub>2</sub> excitation in NGC 2023, Draine & Bertoldi (1996) used a H<sub>2</sub> formation rate  $\sim 1.7$  times larger than the value of  $R_f$  inferred by Jura 1975. In the next section, we discuss the effect of  $R_f$  on the H<sub>2</sub> excitation and emission.

### 3.3. H<sub>2</sub> formation rate

The standard value of the H<sub>2</sub> formation rate,  $R_f$ , has been obtained in diffuse cold clouds from H<sub>2</sub> absorption measurements in the FUV with the Copernicus satellite (Jura 1975): the formation rate found corresponds to  $\gamma = 4.3 \times 10^{-17} \text{ cm}^3 \text{ s}^{-1}$ . The value of  $R_f$  plays an important role in PDR modelling because it controls the location of the H<sup>0</sup>/H<sub>2</sub> transition, i.e., the region of the PDR where a significant H<sub>2</sub> fraction is present and where the gas temperature is still high. Specifically, if  $R_f$  is increased, the H<sup>0</sup>/H<sub>2</sub> transition will move towards the PDR surface where the gas temperature is higher. The enhanced formation rate requires a higher photodissociation rate, i.e., lower  $A_V$ -values, to be in keeping with the balance requirement between formation and destruction. For a PDR with moderate  $\chi$ , such as the  $\rho$  Oph-W, the gas temperature profile is not much affected by

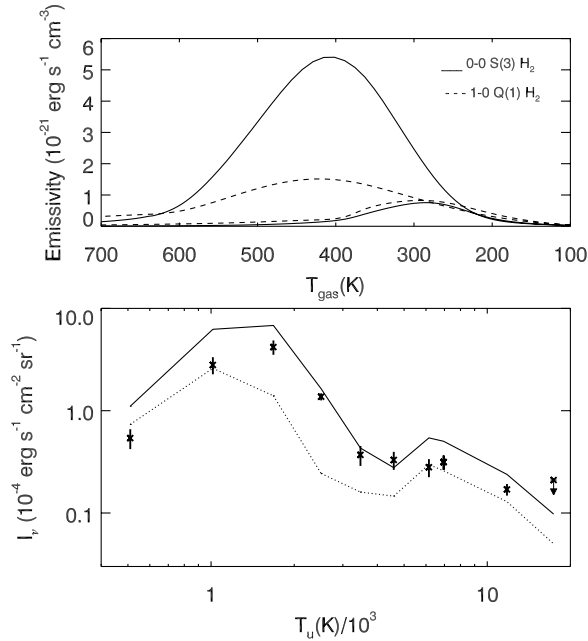


**Fig. 10.** Upper panel: line emission profiles as a function of gas temperature for two H<sub>2</sub> formation rates corresponding to  $\gamma = 2.6 \times 10^{-16} \text{ cm}^3 \text{ s}^{-1}$  (set of curves to the left) and  $\gamma = 4.3 \times 10^{-17} \text{ cm}^3 \text{ s}^{-1}$  (set of curves to the right) as a function of the gas temperature. The lower  $R_f$  is the reference value inferred from Copernicus data. Lower panel: the line intensities of H<sub>2</sub> with error bars as observed (crosses) and predicted for the two H<sub>2</sub> formation rates (solid and dotted lines for the highest and lowest rate respectively), as a function of the upper level energy in Kelvin, at the peak of the H<sub>2</sub> emission (SWS position 2).

the enhancement of  $R_f$  because the dominant heating and cooling mechanisms (photoelectric heating and fine structure line emission of O<sup>0</sup> and C<sup>+</sup>) do not depend on  $R_f$ .

Figure 10 shows the effect of the H<sub>2</sub> formation rate on the line emissivity. A PDR model with a fast formation rate,  $\gamma = 2.6 \times 10^{-16} \text{ cm}^3 \text{ s}^{-1}$ , reproduces relatively well the H<sub>2</sub> line emission observed: as expected the increase of  $R_f$  results in stronger low rotational (higher  $T_{\text{gas}}$ ) and stronger high rotational and rovibrational (higher UV flux) line emission. In this latter model, characterised by a gas temperature profile very similar to the profile presented in Fig. 8, the H<sup>0</sup>/H<sub>2</sub> occurs in the hot gas at  $A_v \approx 0.2$ . Within the H<sub>2</sub> emission layer the excitation of the first few H<sub>2</sub> rotational lines ( $J \lesssim 5$ ) is dominated by collisions (see Fig. 10). Outside this region the contribution of UV pumping followed by fluorescent cascade becomes dominant even for the lowest energy levels. Qualitatively, the contribution of collisional excitation relative to UV pumping decreases inwards because the gas becomes too cold and outwards because the gas density drops. For the PDR model with the fast formation rate, we note nevertheless that the higher UV flux required to explain the emission from the high H<sub>2</sub> rotational states ( $J = 6-7$  mainly populated by UV pumping, see text in Sect. 3.4 and Fig. 12) produces too much emission in the H<sub>2</sub> rovibrational lines ( $v \geq 1$ ).

In Fig. 11 we show the emission profiles of the 0-0 S(3) and 1-0 S(1) lines of H<sub>2</sub> across the interface and compare them with

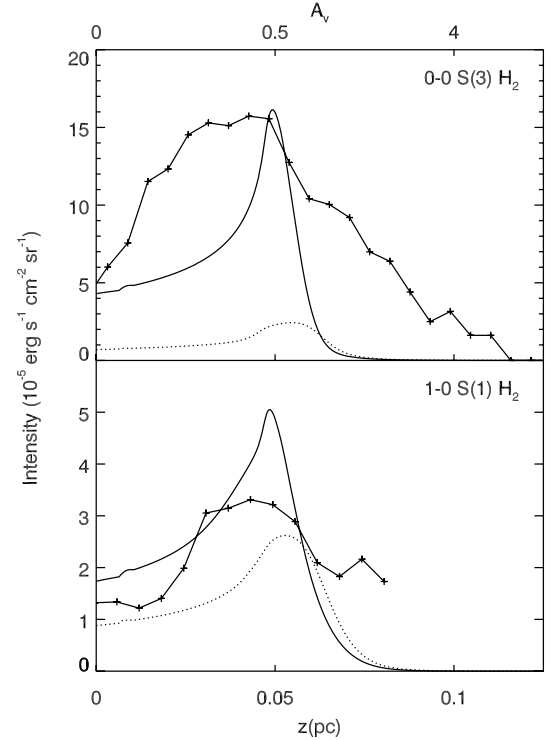


**Fig. 11.** Intensity of the 0-0 S(3) and 1-0 S(1) H<sub>2</sub> lines as observed (solid lines with crosses) and predicted by PDR models with a high,  $\gamma = 2.6 \times 10^{-16} \text{ cm}^3 \text{ s}^{-1}$ , and low,  $\gamma = 4.3 \times 10^{-17} \text{ cm}^3 \text{ s}^{-1}$ ,  $R_f$  (solid and dotted lines respectively), as a function of distant and of visual extinction from the PDR outer edge. The 1-0 S(1) H<sub>2</sub> line brightness (shown in Fig. 5) has been scaled by the PAH emission assuming that the ratio of the H<sub>2</sub> to PAH emission is constant along the filament (see Sect. 2.2.2).

PDR models corresponding to a slow ( $\gamma = 4.3 \times 10^{-17} \text{ cm}^3 \text{ s}^{-1}$ ) and fast ( $\gamma = 2.6 \times 10^{-16} \text{ cm}^3 \text{ s}^{-1}$ ) H<sub>2</sub> formation rate. Again, these profiles cannot be explained by a model with a slow  $R_f$ : they rather require a fast  $R_f$ . However, even in this latter case, the model profile does not reproduce the spatial extent of the emission into the PDR (Fig. 11). We believe that this discrepancy results from the simple spherical geometry adopted in our modelling (Fig. 6). Two filaments appear well separated at several places along the interface. For the observations we have selected the narrowest interface section, where the two filaments appear closer on the sky but probably not exactly aligned along the line of sight. Projection effects resulting from sub-structures might be not negligible and could explain the width of the H<sub>2</sub> line emission profile.

The high  $R_f$  value found here rules out a formation process where two hydrogen atoms physisorbed on the surface of a big grain recombine to form H<sub>2</sub>. Such a mechanism is efficient only in regions moderately irradiated ( $\chi < 100$ ) where the equilibrium temperature of big grains drops below  $\sim 20$  K (Pirronello et al. 1997, 1999; Katz et al. 1999). In the case of the  $\rho$  Oph-W interface, the high temperature of big grains ( $\sim 35$  K) favors thermal evaporation and maintains the physisorption rate of hydrogen at a low value. This suggests that formation of H<sub>2</sub> on big grains (at least in PDRs) involves chemically attached H-atoms. In this second process, H<sub>2</sub> could form by (i) a prompt reaction

of free H atoms from the gas phase with chemisorbed H atoms (Duley 1996; Parneix & Brechignac 1998) or through (ii) the recombination of a physisorbed H with a chemisorbed H atom (Habart 2001; Habart et al. 2002b; Cazaux & Tielens 2002). Considering the fact that small carbonaceous grains make a dominant contribution to the total grain surface and have numerous chemically bonded hydrogen atoms, it is plausible that they play a dominant role in H<sub>2</sub> formation by chemisorption. For H<sub>2</sub> chemisorption formation, the H<sub>2</sub> formation rate can be as high as  $10^{-16}$  cm<sup>3</sup> s<sup>-1</sup> when  $T_{\text{gas}} \sim 300$  K (Habart 2001; Habart et al. 2002b; Cazaux & Tielens 2002). Another possible way of forming H<sub>2</sub> is through the dissociation of PAHs induced by UV light. Léger et al. (1989) have shown that the absorption of a UV photon can sufficiently heat the molecule to cause the ejection of a H<sub>2</sub> fragment. Recent laboratory results (Joblin et al. 2001) on the photodissociation of PAHs isolated in ions traps exposed to UV light are encouraging in this respect. However, if PAHs contribute efficiently to the formation of H<sub>2</sub>, they must be continuously rehydrogenated: this could be the case for larger PAHs where the energy per degree of freedom is lower (Boulanger et al. 1998b; Verstraete et al. 2001).

The spatial distribution of PAHs and H<sub>2</sub> emission is another important hint concerning the coupling of PAHs with H in the ISM. The present spatial correlation found between the PAH and H<sub>2</sub> emission could result not only from the fact that both H<sub>2</sub> and PAHs are excited by UV photons but also from the fact that the illuminated PAHs produce H<sub>2</sub>.

### 3.4. Effect of the abundance of PAHs

In photodissociation regions, dust is intimately coupled to the evolution of gas. First, the grain photoelectric heating is a strong component of the gas heat budget. Second, the formation of H<sub>2</sub> necessarily occurs on dust grains. These processes are sensitive to the size distribution, the nature of the dust grains and, especially, to the abundance of the small particles. Recent theoretical (Bakes & Tielens 1994; Weingartner & Draine 2001) and observational (Habart et al. 2001) work has shown that the photoelectric heating is dominated by the contribution of the small grains (radius  $\leq 100$  Å). Furthermore, former studies have shown that there are abundance variations of the small grains in interstellar clouds (Boulanger et al. 1988; Boulanger et al. 1990; Bernard et al. 1993) and that they have an important impact on the gas heating rate (Habart et al. 2001).

We first estimate the PAH abundance across the  $\rho$  Oph-W interface. Based on the LW2 brightness (see Sect. 3.1) we can determine the PAH abundance across the  $\rho$  Oph-W interface. First, we need to derive the total power emitted by PAHs,  $\epsilon_{\text{PAH}}$ , from the LW2 (5–8.5  $\mu\text{m}$ ) emission. This can be done from the CVF spectra in the 2–15  $\mu\text{m}$  wavelength range of the  $\rho$  Oph-W PDR. We find  $\epsilon_{\text{PAH}} \approx 2 \times \epsilon_{\text{LW2}} \approx 6 \times 10^{-32}$  W/H for the emission of PAHs heated by a B2 star ( $T_{\text{eff}} = 22\,000$  K) and with  $\chi = 1$ . The PAH abundance can now be obtained if we know the power absorbed (or emitted) per C-atom in a PAH,  $P_{\text{C}}$ . Using the PAH absorption cross-section of Verstraete & Léger (1992) and the size distribution described in Sect. 3.2, we find  $P_{\text{C}} \approx 1.5 \times 10^{-27}$  W/C in the radiation field of HD147889 and with

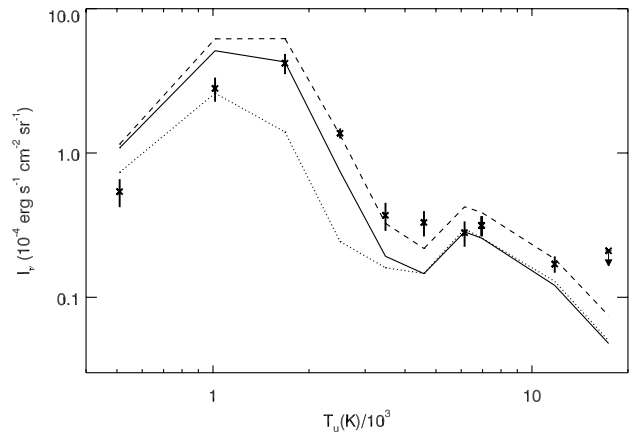


**Fig. 12.** The line intensities of H<sub>2</sub> with error bars as observed (crosses) and predicted by models (lines), as a function of the upper level energy in Kelvin, at the peak of the H<sub>2</sub> emission (SWS position 2). Dotted and solid lines correspond to models with a standard H<sub>2</sub> formation rate inferred from Copernicus data and a carbon abundance in PAHs equal to 0.5 and  $1 \times 10^{-4}$  respectively. The model with a H<sub>2</sub> formation rate corresponding to  $1.3 \times 10^{-16}$  cm<sup>3</sup> s<sup>-1</sup> and a carbon abundance in PAHs equal to  $0.75 \times 10^{-4}$  is represented by the dashed line.

$\chi = 1$ . Finally, the PAH abundance is given by  $[C/H]_{\text{PAH}} = \frac{\epsilon_{\text{PAH}}}{P_{\text{C}}}$  and we find  $[C/H]_{\text{PAH}} \approx 4 \times 10^{-5}$ , which is consistent with the standard value derived in the ISM (see Sect. 3.1).

We now investigate the effect of the PAHs abundance on the H<sub>2</sub> excitation. First, we place ourselves in the extreme case where the PAH emission profile over the  $\rho$  Oph-W interface (see Fig. 7) only reflects variations of the PAH abundance. In this case, the LW2 emission profile is reproduced if we assume a low constant density distribution,  $n_{\text{H}}(r) = 5 \times 10^3$  cm<sup>-3</sup> (for which the LW2 emission profile is not affected by dust extinction), and a PAH abundance which varies by a factor 5 from the cloud edge to the emission peak ( $[C/H]_{\text{PAH}} = 0.2$  to  $1 \times 10^{-4}$ ). The H<sub>2</sub> line emission of the corresponding PDR model underestimates the observed fluxes by a factor about 5. In fact, although the gas temperature is enhanced because of the large PAH abundance, the lower density yields a H<sub>2</sub> abundance too small to account for the SWS observations. We therefore conclude that the PAH abundance cannot vary greatly across the  $\rho$  Oph-W interface. Second, assuming that the PAH abundance is constant, we test the impact of the  $[C/H]_{\text{PAH}}$  value on the H<sub>2</sub> emission lines. Increasing the PAHs abundance by a factor 2 in the PDR modelling ( $[C/H]_{\text{PAH}} \sim 2 \times 5 \times 10^{-5}$ ), we obtain the result displayed in Fig. 12. The populations of the lowest rotational levels ( $J \leq 5$ ) of H<sub>2</sub> have been strongly enhanced: this is a result of an enhanced photoelectric heating rate which translates into a higher gas temperature (by a factor 2) in the H<sup>0</sup>/H<sub>2</sub> transition. On the other hand, the populations and emission from the higher rotational ( $J > 5$ ) and rovibrational states of H<sub>2</sub> which are UV pumped have not been much affected. In the hypothesis where H<sub>2</sub> forms on PAHs, the H<sub>2</sub> formation rate  $R_{\text{f}}$  should scale with the PAH abundance as does the photoelectric heating rate. We therefore run a model where  $R_{\text{f}}$  changes proportionally to the PAH abundance. This model with  $\gamma = 1.3 \times 10^{-16}$  cm<sup>3</sup> s<sup>-1</sup> and  $[C/H]_{\text{PAH}} = 0.75 \times 10^{-4}$  reproduces well the spectroscopic data (see Fig. 12). However,

as it is unclear how H<sub>2</sub> forms in the ISM, this plausible relation between the H<sub>2</sub> formation rate and the PAH abundance is not warranted.

We conclude that a H<sub>2</sub> formation rate of at least  $R_f \sim 1 \times 10^{-16} \text{ cm}^3 \text{ s}^{-1}$  at 330 K (e.g.,  $\gamma \sim 1.3 \times 10^{-16} \text{ cm}^3 \text{ s}^{-1}$  or  $\sim 3$  times that of Jura 1975) is required to account for the observed H<sub>2</sub> emission lines.

It must be emphasized that this conclusion was reached in the case of a static, equilibrium PDR. In reality, advection motions (due to the propagation of the photodissociation front and/or the presence of turbulent velocity fields) may exist in the  $\rho$  Oph-W interface. Recent modeling of out-of-equilibrium PDRs has shown that the H<sub>2</sub> line emission can be enhanced by factors about 3 for an advection velocity of  $1 \text{ km s}^{-1}$  (Stoerzer & Hollenbach 1998).

We discuss below the importance of advection qualitatively. In the case of the  $\rho$  Oph-W PDR, the dissociation front propagates at a maximal velocity  $v_a \sim 0.7 \text{ km s}^{-1}$  (Bertoldi & Draine 1996). Thus, for the H<sub>2</sub> abundance profile reproducing observations, we can estimate the advection rate  $\vec{v}_a \cdot \vec{\nabla} n_{\text{H}_2}$  (which is equivalent to a local H<sub>2</sub> formation rate). Because of the relative high density gradient of the interface, the advection rate in the H<sub>2</sub> emission layer,  $\vec{v}_a \cdot \vec{\nabla} n_{\text{H}_2} \sim 10^{-6} \text{ cm}^{-3} \text{ s}^{-1}$ , is much larger than the H<sub>2</sub> photodissociation rate,  $R_{\text{diss}} \sim 10^{-8} \text{ cm}^{-3} \text{ s}^{-1}$ . If this were the case the H<sup>0</sup>/H<sub>2</sub> transition would occur at very low optical depth where the gas is hot ( $T_{\text{gas}} > 500 \text{ K}$ , see Fig. 8). Since the H<sub>2</sub> emission we observe comes from a colder layer ( $T_{\text{gas}} \sim 300\text{--}345 \text{ K}$ ), we believe that advection motions cannot play a major role in the formation of line intensities. However, out-of-equilibrium modeling for the  $\rho$  Oph-W PDR physical conditions is warranted to estimate quantitatively the effect of advection. In addition, observations at high spatial and spectral resolution should be used to trace the velocity field of advection motions.

### 3.5. Ortho-to-para H<sub>2</sub> ratio

The ortho-to-para H<sub>2</sub> ratio  $R_{\text{op}}$  suggested by the spectroscopic data (see Sect. 2.2.1) is much lower than the equilibrium value computed in the model  $\sim 3$  for  $T_{\text{gas}} \sim 300\text{--}345 \text{ K}$ . This discrepancy points at the importance of out-of-equilibrium processes. The mechanisms which control the ortho-to-para ratio in PDRs are:

1. gas-phase spin exchange reactions: in warm gas, this conversion arises from reaction between H and H<sub>2</sub>, and in cool gas by the reaction of H<sub>2</sub> with H<sup>+</sup> and H<sub>3</sub><sup>+</sup>;
2. H<sub>2</sub>-grain collisions (Le Bourlot 2000);
3. formation of H<sub>2</sub> on grain surfaces is expected to lead to  $R_{\text{op}}$  equal to 3. But if the newly formed H<sub>2</sub> resides long enough on the grain, process (2) might be more important (Chrysostomou et al. 1993).

Our low  $R_{\text{op}}$  confirms former studies on photodissociation regions where the gas is excited mostly by starlight. ISO-SWS observations towards other PDRs (as NGC 2023 or NGC 7023, Moutou et al. 1999; Fuente et al. 2000), have provided evidence of non equilibrium  $R_{\text{op}}$ . Presently, two scenarios are proposed

to explain the observed low  $R_{\text{op}}$  values. First, fast conversion of ortho-H<sub>2</sub> in para-H<sub>2</sub> can occur on the surface of non magnetic, non metallic grains (Le Bourlot 2000). The fraction of H<sub>2</sub> converted depends on the ratio of the characteristic conversion time (of the order of one minute) to the residence time of physisorbed H<sub>2</sub>, which critically depends on the grain temperature and the adsorption binding energy of H<sub>2</sub>. Alternatively, the low  $R_{\text{op}}$  observed can be the legacy of rapid advection of molecular cold gas ( $T_{\text{gas}} \leq 90 \text{ K}$ ) from the shielded region into the surface zone. For the physical conditions in the H<sub>2</sub> emitting layer of the  $\rho$  Oph-W PDR, the dominant conversion process between ortho and para H<sub>2</sub> in the gas is the reaction with H<sup>+</sup> and H<sub>3</sub><sup>+</sup> characterised by a time scale of  $1.9 \times 10^4 \text{ yr}$  (Schofield 1967). Therefore, based on the 0.02 pc thickness of the H<sub>2</sub> emitting layer of the plane-parallel model, we find that the advection speed has to be of the order of  $1 \text{ km s}^{-1}$  or larger to deviate  $R_{\text{op}}$  from its equilibrium value. This is a reasonable value which could be accounted for by turbulent motions and/or progression of the photodissociation front into the cloud (see Sect. 3.4). Again, modeling of out-of-equilibrium PDRs and high spectral resolution observations are required to discriminate the two above scenarios for non-equilibrium  $R_{\text{op}}$  values.

### 3.6. Fine structure lines

The gas in PDRs is cooled by far-infrared fine-structure lines, such as [CII] 158  $\mu\text{m}$ , [OI] 63, 146  $\mu\text{m}$ , [SiII] 35  $\mu\text{m}$ , [CI] 609, 370  $\mu\text{m}$ , and by molecular rotational lines, particularly of H<sub>2</sub> and CO. To test our understanding of the gas cooling in PDRs, we also confront predicted and observed fine structure line intensities. In the PDR model, we use recent gas phase elemental abundances measured in the diffuse interstellar medium: He/H = 0.1, C/H =  $1.4 \times 10^{-4}$  (Cardelli et al. 1996), O/H =  $3.19 \times 10^{-4}$  (Meyer et al. 1998), and Si/H =  $1.78 \times 10^{-6}$  (Cardelli et al. 1994). In Table 2, we compare the observed line intensities of the major coolants diluted in the  $\sim 80''$  beam of LWS (see Fig. 1) to the predictions of the different PDR models presented in Sects. 3.2, 3.3 and 3.4. Agreement is generally good between observations and model predictions. Note that the [O<sup>0</sup>] 63  $\mu\text{m}$  emission is particularly sensitive to the cloud geometry and total opacity (see Sect. 3.2). This dependence arises from transfert effects on this line, which is optically thick for  $A_v \geq 0.3$ , with a turbulent Doppler width of  $1 \text{ km s}^{-1}$  (Tielens & Hollenbach 1985). The fine structure line intensities are not affected by changes of the H<sub>2</sub> formation rate, but depend on the abundance of small dust grains. In the model where the PAH abundance is increased by a factor 2, the C<sup>+</sup>, O<sup>0</sup> and Si<sup>+</sup> lines emission are enhanced by  $\sim 50\%$  at most. As such variations fall within our error bars on the gas cooling lines ( $\sim 30\%$  on the observed flux more uncertainties on the opacity correction), the confrontation between fine-structure lines emission as observed and as predicted cannot permit us to discriminate between these different PDR models. The comparison of the power radiated by PAHs and gas allows us to measure the PAHs photoelectric efficiency. We find  $\epsilon_{\text{PAH}} \sim 4\%$ , which is in good agreement with recent theoretical estimates

**Table 2.** Average intensities radiated by gas coolants and PAHs towards the  $\rho$  Oph-W PDR (all the SWS intensities have been diluted in the  $\sim 80''$  beam of LWS).

Species	Intensity <sup>a</sup> :	Observed	Model A <sup>1</sup>	B <sup>2</sup>	C <sup>3</sup>	D <sup>4</sup>
[C <sup>+</sup> ] 158 $\mu\text{m}$ (LWS)		$3.0 \pm 0.3 \times 10^{-4}$	$2.5 \times 10^{-4}$	$2.4 \times 10^{-4}$	$3 \times 10^{-4}$	$2.7 \times 10^{-4}$
[O <sup>0</sup> ] 63 $\mu\text{m}$ (LWS)		$6.5 \pm 2.3 \times 10^{-5}$	$6.1 \times 10^{-5}$	$5.9 \times 10^{-5}$	$9.1 \times 10^{-5}$	$7.1 \times 10^{-5}$
[O <sup>0</sup> ] 146 $\mu\text{m}$ (LWS)		$1.4 \pm 0.4 \times 10^{-4}$	$2.2 \times 10^{-4}$	$2.5 \times 10^{-4}$	$3.4 \times 10^{-4}$	$2.9 \times 10^{-4}$
[Si <sup>+</sup> ] 35 $\mu\text{m}$ (SWS)		$3.2 \pm 0.3 \times 10^{-5}$	$1.2 \times 10^{-4}$	$1.0 \times 10^{-4}$	$1.7 \times 10^{-4}$	$1.3 \times 10^{-4}$
H <sub>2</sub> <sup>b</sup> (SWS)		$6.5 \pm 0.7 \times 10^{-4}$	$2.8 \times 10^{-4}$	$8.7 \times 10^{-4}$	$5.5 \times 10^{-4}$	$7.7 \times 10^{-4}$
Total gas cooling		$1.2 \times 10^{-3}$	$0.9 \times 10^{-3}$	$1.5 \times 10^{-3}$	$1.4 \times 10^{-3}$	$1.5 \times 10^{-3}$
$I_{\text{PAH}}(2\text{--}15 \mu\text{m})$ (ISOCAM)		0.03	0.028	0.028	0.056	0.042
$\epsilon_{\text{PE}}$		0.04	0.032	0.053	0.025	0.036

<sup>a</sup> In  $\text{erg s}^{-1} \text{cm}^{-2} \text{sr}^{-1}$ .

<sup>b</sup> Sum of the H<sub>2</sub> lines observed.

<sup>1</sup> Model with  $\gamma = 4.3 \times 10^{-17} \text{cm}^3 \text{s}^{-1}$  (see Sect. 3.2) and  $[\text{C}/\text{H}]_{\text{PAH}} = 0.5 \times 10^{-4}$ .

<sup>2</sup> Model with  $\gamma = 2.6 \times 10^{-16} \text{cm}^3 \text{s}^{-1}$  and  $[\text{C}/\text{H}]_{\text{PAH}} = 0.5 \times 10^{-4}$ .

<sup>3</sup> Model with  $\gamma = 4.3 \times 10^{-17} \text{cm}^3 \text{s}^{-1}$  and  $[\text{C}/\text{H}]_{\text{PAH}} = 1 \times 10^{-4}$ .

<sup>4</sup> Model with  $\gamma = 1.3 \times 10^{-16} \text{cm}^3 \text{s}^{-1}$  and  $[\text{C}/\text{H}]_{\text{PAH}} = 0.75 \times 10^{-4}$ .

(Bakes & Tielens 1994; Weingartner & Draine 2001) and observational values (Habart et al. 2001). Note that the spatial correlation between emission from PAH and from collisionally excited H<sub>2</sub> (see Sect. 2.2) points out the role of UV light through photoelectric effect on small grains in heating the gas.

#### 4. Conclusion

We study the gas and dust emission across the edge of the  $\rho$  Ophiuchi main cloud illuminated by a B2 star ( $\chi \sim 400$ ). Imaging observations of dust and gas have been obtained with the ISO camera and the ESO ground-based telescope at La Silla. ISO-SWS and -LWS measurements provide the emission of rotational and rovibrational lines of H<sub>2</sub> and of fine structure lines of C<sup>+</sup> and O<sup>0</sup>. Thanks to its proximity, its relative simple geometry and its moderate gas density ( $n_{\text{H}} \simeq 10^4 \text{cm}^{-3}$ ), the structure of the  $\rho$  Oph-W PDR is resolved and we observe a spatial correlation between the small dust and the collisionally excited as well as the fluorescent H<sub>2</sub> emission.

The comparison between observations and model predictions allows us to test our understanding of the physics of photodissociation regions. At small scale within the cloud ( $\sim 0.005 \text{pc}$ ), we have been able to connect the geometry, the physical conditions and the penetration of the ultraviolet light through the cloud to the dust and gas emission profiles. The PAH emission profile gives constraints on the gas density at the edge of the molecular cloud. We derive the gas temperature from the H<sub>2</sub> rotational level populations:  $T_{\text{gas}} = 300\text{--}345 \text{K}$  prevail in a portion of the PDR where significant H<sub>2</sub> is present. The strong constraints provided by ISO on the physical conditions ( $n_{\text{H}}, T_{\text{gas}}$ ) enable us to study in detail the dominant physical processes at work in PDRs. In particular, a high H<sub>2</sub> formation rate in warm gas,  $R_{\text{f}} \gtrsim 1 \times 10^{-16} \text{cm}^3 \text{s}^{-1}$  at  $T_{\text{gas}} = 330 \text{K}$  (e.g.,  $\gamma \gtrsim 1.3 \times 10^{-16} \text{cm}^3 \text{s}^{-1}$  or  $\gtrsim 3$  times that of Jura 1975), is required to account for the H<sub>2</sub> emission lines. It suggests that H<sub>2</sub> forms via chemisorption on the surface of PAHs. In

this interpretation of the H<sub>2</sub> excitation the spatial correlation observed between the PAH and the H<sub>2</sub> emission results not only from the fact that both particules are excited by UV photons but also from the fact that the illuminated PAHs would produce H<sub>2</sub>. A consequence of this scenario is that both the photoelectric heating rate (of PAHs) and the H<sub>2</sub> formation rate could scale with the PAH abundance. In particular, increasing the PAH abundance would lead to a higher gas temperature and would bring the H<sup>0</sup>/H<sub>2</sub> transition closer to the PDR: this could significantly enhance the fluorescent and rotational emission of H<sub>2</sub>. Theoretical and laboratory studies on the H<sub>2</sub> formation process, in conjunction with observations of H<sub>2</sub> and dust emission in the ISM, are currently underway and will provide insight into the formation of molecular hydrogen, a key quantity for our understanding of the ISM.

*Acknowledgements.* We are grateful to Pierre Cox for letting us use his ISO-LWS data on fine-structure emission lines. We also thank the MPE-SDC (Garching) and the DIDAC (Groningen) for their constant support in the data reduction phase and with the use of SWS-IA3. SWS-IA3 is a joint development of the SWS consortium. Contributing institutes are SRON, MPE, KUL and the ESA Astrophysics division.

#### References

- Abergel, A., Bernard, J. P., Boulanger, F., et al. 1996, *A&A*, 315, L329
- Abergel, A., Andre, P., Bacmann, A., et al. 1999, Spatial distribution of dust from cirrus to dense clouds, in *The Universe as seen by ISO*, 615
- An, J. H., & Sellgren, K. 2001, *Astronomy and Astrophysics Series* (Ed. Pachart Publishing Hous Tucson), 198, 5914
- Bakes, E. L. O., & Tielens, A. G. G. M. 1994, *ApJ*, 427, 822
- Bernard, J. P., Boulanger, F., & Puget, J. L. 1993, *A&A*, 277, 609
- Bertoldi, F., & Draine, B. T. 1996, *ApJ*, 458, 222
- Bertoldi, F. 1997, Iso: A novel look at the photodissociated surfaces of molecular clouds (invited paper), in *First ISO Workshop on Analytical Spectroscopy*, 67

- Bontemps, S., Nordh, L., Olofsson, G., et al. 1998, Isocam survey of the rho oph young stellar population, ed. P. Cox, & M. Kessler (The Universe as seen by ISO), 141
- Boulanger, F., & Perault, M. 1988, ApJ, 330, 964
- Boulanger, F., Beichman, C., Desert, F. X., et al. 1988, ApJ, 332, 328
- Boulanger, F., Falgarone, E., Puget, J. L., & Helou, G. 1990, ApJ, 364, 136
- Boulanger, F., Reach, W. T., Abergel, A., et al. 1996, A&A, 315, L325
- Boulanger, F., Abergel, A., Bernard, J. P., et al. 1998, The nature of small interstellar dust particles, in Star formation with the Infrared Space Observatory, 15
- Boulanger, F., Abergel, A., Bernard, J. P., et al. 1998, The nature of small interstellar dust particles, in Star Formation with the Infrared Space Observatory, 15
- Boulanger, F., Boissel, P., Cesarsky, D., & Ryter, C. 1998c, A&A, 339, 194
- Boulanger, F. 1998, Small dust particles in the ism in Solid interstellar matter: The ISO revolution
- Burke, J. R., & Hollenbach, D. J. 1983, ApJ, 265, 223
- Cardelli, J. A., Sofia, U. J., Savage, B. D., Keenan, F. P., & Dufton, P. L. 1994, ApJ, 420, L29
- Cardelli, J. A., Meyer, D. M., Jura, M., & Savage, B. D. 1996, ApJ, 467, 334
- Cazaux, S., & Tielens, A. G. G. M. 2002, ApJ, 575, L29
- Chrysostomou, A., Brand, P. W. J. L., Burton, M. G., & Moorhouse, A. 1993, MNRAS, 265, 329
- De Graauw, T., Haser, L. N., Beintema, D. A., et al. 1996, A&A, 315, L49
- Désert, F. X., Boulanger, F., & Puget, J. L. 1990, A&A, 237, 215
- Draine, B. T., & Bertoldi, F. 1996, ApJ, 468, 269
- Draine, B., & Bertoldi, F. 2000, Theoretical models of photodissociation fronts, in H<sub>2</sub> in Space, 131
- Draine, B. T. & Li, A. 2001, ApJ, 551, 807
- Draine, B. T. 1989, Interstellar extinction in the infrared, in Infrared Spectroscopy in Astronomy, 93
- Duley, W. W., & Williams, D. A. 1984, Interstellar chemistry, in Interstellar Chemistry
- Duley, W. W. 1996, MNRAS, 279, 591
- Dwek, E., Arendt, R. G., Fixsen, D. J., et al. 1997, ApJ, 475, 565
- Federman, S. R., Glassgold, A. E., & Kwan, J. 1979, ApJ, 227, 466
- Field, D., Lemaire, J. L., Pineau Des Forêts, G., et al. 1998, A&A, 333, 280
- Fitzpatrick, E. L., & Massa, D. 1988, ApJ, 328, 734
- Fuente, A., Martin-Pintado, J., & Rodriguez-Fernandez, N. 1999, ApJ, 518, L45
- Fuente, A., Martin Pintado, J., & Rodriguez Fernacute 2000, A&A, 354, 1053
- Habart, E., Verstraete, L., Boulanger, F., et al. 2001, A&A, 373, 702
- Habart, E. 2001, Ph.D Thesis, Couplage entre le gaz et les grains dans le milieu interstellaire (University of Paris 7)
- Habart, E., Abergel, A., Boulanger, F., & Verstraete, L. 2002a, in preparation
- Habart, E., Boulanger, F., Verstraete, L., Pineau des Forêts, G., & Walmsley, M. 2002b, in preparation
- Habing, H. J. 1968, Bull. Astron. Inst. Netherlands, 19, 421
- Hollenbach, D., & Salpeter, E. E. 1971, ApJ, 163, 155
- Hollenbach, D. J., & Tielens, A. G. G. M. 1999, Rev. Mod. Phys., 71, 173
- Joblin, C., Maillard, J. P., De Peslouan, P., et al. 2000, Probing the connection between pabs and hydrogen in the interstellar medium and in the laboratory, in Molecular Hydrogen in Space (Cambridge University Press), 107
- Joblin, C., Boissel, P., Pech, C., Armengaud, M., & Frabel, P. 2001, A piece of interstellar medium in the laboratory: The *pirenea* experiment, in Infrared and Submillimeter Space Astronomy (EDP Sciences)
- Jura, M. 1975, ApJ, 197, 575
- Katz, N., Furman, I., Biham, O., Pirronello, V., & Vidali, G. 1999, ApJ, 522, 305
- Kelsall, T., Weiland, J. L., Franz, B. A., et al. 1998, ApJ, 508, 44
- Kessler, M. F., Steinz, J. A., Anderegg, M. E., et al. 1996, A&A, 315, L27
- Le Boulrot, J., Pineau des Forêts, G., Roueff, E., & Flower, D. R. 1993, A&A, 267, L233
- Le Boulrot, J., Pineau des Forêts, G., & Flower, D. R. 1999, MNRAS, 305, L802
- Le Boulrot, J. 2000, A&A, 360, L656
- Le Coupanec, P. 1998, Ph.D. Thesis, Observations et modelisation des Bandes Diffuses et Bandes Infrarouges dans le milieu interstellaire: Confrontation a l'hypothese PAH (University of Paris 6)
- Léger, A., D'Hendecourt, L., Boissel, P., & Desert, F. X. 1989, A&A, 213, L351
- Lemaire, J. L., Field, D., Gerin, M., et al. 1996, A&A, 308, L895
- Li, A., & Draine, B. T. 2001, ApJ, 554, L778
- Liseau, R., White, G. J., Larsson, B., et al. 1999, A&A, 344, L342
- Loren, R. B. 1989, ApJ, 338, L902
- Meyer, D. M., Jura, M., & Cardelli, J. A. 1998, ApJ, 493, 222
- Moutou, C., Verstraete, L., Sellgren, K., & Léger, A. 1999, The rich spectroscopy of reflection nebulae, in The Universe as Seen by ISO, 727
- Parmar, P. S., Lacy, J. H., & Achtermann, J. M. 1991, ApJ, 372, L25
- Parneix, P., & Brechignac, P. 1998, A&A, 334, 363
- Pirronello, V., Liu, C., Shen, L., & Vidali, G. 1997, ApJ, 475, L69
- Pirronello, V., Liu, C., Roser, J. E., & Vidali, G. 1999, A&A, 344, 681
- Puget, J. L., Léger, A., & Boulanger, F. 1985, A&A, 142, L19
- Rouan, D., Field, D., Lemaire, J. L., et al. 1997, MNRAS, 284, 395
- Schofield, K. 1967, Planet. Space Sci., 643, 15
- Sellgren, K., Allamandola, L. J., Bregman, J. D., Werner, M. W., & Wooden, D. H. 1985, ApJ, 299, 416
- Stoerzer, H., & Hollenbach, D. 1998, ApJ, 495, 853
- Tielens, A. G. G. M., & Hollenbach, D. 1985, ApJ, 291, 722
- Timmermann, R., Bertoldi, F., Wright, C. M., et al. 1996, A&A, 315, L281
- Valentijn, E. A., Feuchtgruber, H., Kester, D. J. M., & Roelfsema, P. R. 1996, A&A, 315, L60
- Verstraete, L., & Léger, A. 1992, A&A, 266, 513
- Verstraete, L., Pech, C., Moutou, C., et al. 2001, A&A, 372, 981
- Weingartner, J. C., & Draine, B. T. 2001, ApJS, 134, 263